

Viscosity-dominated hydraulic fractures

E. Detournay

University of Minnesota, Minneapolis, USA

A. P. Peirce

University of British Columbia, Vancouver, Canada

A. P. Bunger

CSIRO Petroleum, Melbourne, Australia

ABSTRACT: Using scaling arguments, this paper first demonstrates that most hydraulic fracturing treatments are in the viscosity-dominated regime; i.e., the evolution of the fracture during fluid injection does not depend on the rock toughness, a material parameter quantifying the energy required to break the rock. In the viscosity-dominated regime, the aperture in the crack tip region (viewed at the fracture scale) is no longer characterized by the classical square root behavior predicted by linear elastic fracture mechanics, since other asymptotic behaviors prevail. For example, under conditions of large efficiency and small fluid lag, the asymptotic tip aperture that reflects the predominance of viscous dissipation is of the form $w \sim s^{2/3}$ (where s is the distance from the tip). The physical reality of the viscosity-dominated regime is confirmed by results of laboratory experiments where radial hydraulic fractures were propagated by injecting aqueous solutions of glycerin or glucose along an epoxy-bonded interface between two Polymethyl Methacrylate (PMMA) blocks. Agreement to within 10 percent is demonstrated between the experimental results for the location of the fracture front and the full-field fracture opening (measured using a novel optical technique), and the semi-analytical solution of a radial hydraulic fracture propagating in a zero toughness impermeable elastic material. Finally, we demonstrate that provided the appropriate tip behavior is embedded in the algorithm, a planar hydraulic fracture simulator with a rather coarse mesh is able to accurately reproduce the semi-analytical solution for a radial hydraulic fracture propagating in the viscosity-dominated regime.

1 INTRODUCTION

Fluid-driven fractures represent a particular class of tensile fractures that propagate in solid media, typically under preexisting compressive stresses, as a result of internal pressurization by an injected viscous fluid. Hydraulic fractures are most commonly engineered for the stimulation of hydrocarbon-bearing rock strata to increase production of oil and gas wells (Economides & Nolte 2000), but there are other industrial applications such as remediation projects in contaminated soils (Murdoch 2002), waste disposal (Abou-Sayed 1994), preconditioning and cave inducement in mining (Jeffrey & Mills 2000). Furthermore, hydraulic fractures manifest at the geological scale as kilometer-long vertical dikes bringing magma from deep underground chambers to the earth's surface (Lister & Kerr 1991, Rubin 1995), or as subhorizontal fractures known as sills that divert magma from dikes (Pollard & Hozlhausen 1979).

Since the pioneering work by Khristianovic &

Zhel'tov (1955), there have been numerous contributions to the modeling of fluid-driven fractures that have been mainly motivated by the application of hydraulic fracturing to the stimulation of oil and gas wells, see e.g. Bunger et al. (2007) for a comprehensive list of references.

Most of the hydraulic fracture simulators that are freed of *a priori* constraints on the fracture shape and of the approximations associated with models commonly referred to as "Pseudo-3D," are based on linear elastic fracture mechanics (LEFM); this is reflected by the imposition of a square root asymptotic behavior on the fracture aperture, $w \sim s^{1/2}$ in the tip region (where s is the distance from the crack front). As is well known, the square root asymptote is intimately linked to the energy dissipated in the creation of new fracture surfaces in the rock (Rice 1968). However, it was progressively realized in the late 1980's and early 1990's (Spence & Sharp 1985, Lister 1990, Desroches et al. 1994) that other tip asymptotes (e.g., of the form $w \sim s^{2/3}$ for a Newtonian fluid and in the absence of

leak-off) arise under conditions where the energy in the tip region of a propagating fracture is essentially dissipated in viscous flow. These results have motivated in part the construction of accurate solutions for plane strain and penny-shaped fractures propagating in the viscosity-dominated regime (Savitski & Detournay 2002, Adachi & Detournay 2002, Garagash & Detournay 2005, Garagash 2006, Adachi & Detournay 2007, Madyarova & Detournay 2007, Mitchell et al. 2006).

In this paper, we first demonstrate that most hydraulic fracturing treatments are indeed in the viscosity-dominated regime. We then report the results of experiments, where radial hydraulic fractures were propagated in the viscosity-dominated regime by injecting aqueous solutions of glycerin or glucose along an epoxy-bonded interface between two PMMA blocks. The fluids contained blue dye and the fracture aperture was measured using a technique that relies on analyzing the reduction of the light intensity on the passage of light from a backlight source through the fluid-filled fracture. Agreement to within 10 percent is demonstrated between the experimental results for the location of the fracture front and the full-field fracture opening, and the semi-analytical solution for a radial hydraulic fracture propagating in a zero toughness impermeable elastic material. Finally, we demonstrate that provided the $w \sim s^{2/3}$ tip behavior is embedded in the algorithm, a hydraulic fracture simulator with a rather coarse mesh is able to accurately reproduce the semi-analytical solution.

2 MATHEMATICAL MODEL

Mathematical models of hydraulic fractures propagating in permeable rocks have to account for the primary physical mechanisms involved, namely, deformation of the rock, fracturing or creation of new surfaces in the rock, flow of viscous fluid in the fracture, and leak-off of the fracturing fluid into the permeable rock. The material parameters quantifying these processes correspond to the Young's modulus E and Poisson's ratio ν , the rock toughness K_{Ic} , the fracturing fluid viscosity μ (assuming a Newtonian fluid), and the leak-off coefficient C_l , respectively.

In principle, there is also a lag λ between the front of the fracturing fluid and the crack edge, which depends, among other parameters, on the magnitude of the in-situ stress and the pore pressure. However, a parametric analysis indicates that the lag can be ignored for most hydraulic fracturing treatments (Bunger & Detournay 2007).

The problem of a radial hydraulic fracture, driven by injecting a viscous fluid from a "point-source" at a constant volumetric rate Q_o , is schematically shown in Figure 1. Under conditions where the lag is negligible ($\lambda/R \ll 1$), determining the solution of this problem consists of finding the aperture w of the frac-

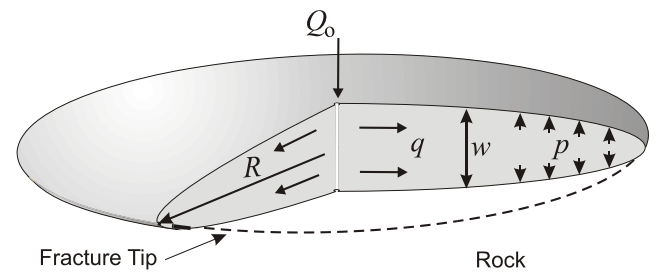


Figure 1. Radial hydraulic fracture.

ture, and the net pressure p (the difference between the fluid pressure p_f and the far-field stress σ_o) as a function of both the radial coordinate r and time t , as well as the evolution of the fracture radius $R(t)$. The functions $R(t)$, $w(r, t)$, and $p(r, t)$ depend on the injection rate Q_o and on the four material parameters E' , μ' , K' , and C' respectively defined as

$$\begin{aligned} E' &= \frac{E}{1 - \nu^2} & \mu' &= 12\mu \\ K' &= \left(\frac{32}{\pi}\right)^{1/2} K_{Ic} & C' &= 2C_l \end{aligned} \quad (1)$$

The three functions $R(t)$, $w(r, t)$, and $p(r, t)$ are determined by solving a system of equations which can be summarized as follows:

- *Elasticity equation:*

$$w = \frac{R}{E'} \int_0^1 G(r/R, s) p(sR, t) s ds \quad (2)$$

where G is a known elastic kernel Sneddon (1951). This singular integral equation expresses the non-local dependence of the fracture width w on the net pressure p .

- *Lubrication equation:*

$$\frac{\partial w}{\partial t} + g = \frac{1}{\mu'} \frac{1}{r} \frac{\partial}{\partial r} \left(r w^3 \frac{\partial p}{\partial r} \right) \quad (3)$$

This non-linear partial differential equation governs the flow of a viscous incompressible fluid inside the fracture Batchelor (1967). The function $g(r, t)$ denotes the rate of fluid leak-off, which evolves according to

$$g = \frac{C'}{\sqrt{t - t_o(r)}} \quad (4)$$

where $t_o(r)$ is the exposure time of point r (i.e., the time at which the fracture front was at a distance r from the injection point). The leak-off law (4) is an approximation with the constant C' lumping various small scale processes. In general, (4) can be defended under conditions where the leak-off diffusion length is small compared to the fracture length.

- *Global volume balance:*

$$Q_o t = 2\pi \int_0^R w r dr + 2\pi \int_0^t r \int_0^{R(\tau)} g(r, \tau) dr d\tau \quad (5)$$

This equation expresses the fact that the total volume of fluid injected is equal to the sum of the fracture volume and the volume of fluid lost into the rock surrounding the fracture.

- *Propagation criterion:*

$$w \sim \frac{K'}{E'} \sqrt{R-r}, \quad 1 - \frac{r}{R} \ll 1 \quad (6)$$

Within the framework of linear elastic fracture mechanics, this equation embodies the fact that the fracture is always propagating and that energy is dissipated continuously in the creation of new surfaces in rock. Obviously (6) implies that $w = 0$ at the tip.

- *Tip conditions:*

$$w^3 \frac{\partial p}{\partial r} = 0, \quad r = R \quad (7)$$

This zero fluid flow rate condition ($q = 0$) at the fracture tip is applicable only if the fluid completely fills the fracture (including the tip region) or if the lag is negligible at the scale of the fracture.

3 MULTIPLE TIME SCALES

We now summarize the scaling laws for a finite radial fracture driven by a fluid injected at a constant rate (Detournay & Garagash 2007), as these are the key to the understanding of the different regimes of propagation.

Propagation of a hydraulic fracture with zero lag is governed by two competing dissipative processes associated with fluid viscosity and solid toughness, respectively, and two competing components of the fluid balance associated with fluid storage in the fracture and fluid storage in the surrounding rock (leak-off). Consequently, limiting propagation regimes can be associated with the dominance of one of the two dissipative processes and/or the dominance of one of the two fluid storage mechanisms. Thus, we can identify *four primary asymptotic regimes* of hydraulic fracture propagation (with zero lag) where one of the two dissipative mechanisms and one of the two fluid storage components are vanishing: storage-viscosity (M), storage-toughness (K), leak-off-viscosity (\tilde{M}), and leak-off-toughness (\tilde{K}) dominated regimes. For

example, in the storage-viscosity-dominated regime (M), fluid leak-off is negligible compared to fluid storage in the fracture and the energy expended in fracturing the rock is negligible compared to viscous dissipation. The solution in the storage-viscosity-dominated limiting regime is given by the zero-toughness, zero-leak-off solution ($K' = C' = 0$).

Consider the general scaling of a finite fracture which hinges on defining the dimensionless crack opening $\Omega(\rho; \mathcal{P}_1, \mathcal{P}_2)$, net pressure $\Pi(\rho; \mathcal{P}_1, \mathcal{P}_2)$, and fracture radius $\gamma(\mathcal{P}_1, \mathcal{P}_2)$ as (Detournay 2004, Detournay & Garagash 2007)

$$w = \varepsilon L \Omega, \quad p = \varepsilon E', \quad R = \gamma L \quad (8)$$

With these definitions, we have introduced the scaled coordinate $\rho = r/R(t)$ ($0 \leq \rho \leq 1$), a small number $\varepsilon(t)$, a length scale $L(t)$ of the same order of magnitude as the fracture length $R(t)$, and two dimensionless evolution parameters $\mathcal{P}_1(t)$ and $\mathcal{P}_2(t)$, which depend monotonically on t .

Four different scalings can be defined in connection to the four primary limiting cases introduced earlier. These scalings yield power law dependence of L , ε , \mathcal{P}_1 , and \mathcal{P}_2 on time t ; i.e. $L \sim t^\alpha$, $\varepsilon \sim t^\delta$, $\mathcal{P}_1 \sim t^{\beta_1}$, $\mathcal{P}_2 \sim t^{\beta_2}$, see Table 1 for the case of a radial fracture. Furthermore, the evolution parameters can take either the meaning of a toughness ($\mathcal{K}_m, \mathcal{K}_{\tilde{m}}$), or a viscosity ($\mathcal{M}_k, \mathcal{M}_{\tilde{k}}$), or a storage ($\mathcal{S}_{\tilde{m}}, \mathcal{S}_{\tilde{k}}$), or a leak-off coefficient ($\mathcal{C}_m, \mathcal{C}_k$).

Table 1. Small parameter ε , lengthscale L for the two storage scalings (viscosity and toughness) and the two leak-off scalings (viscosity and toughness).

| Scaling | ε | L |
|--|--|---|
| storage/ viscosity (M) | $\left(\frac{\mu'}{E't}\right)^{1/3}$ | $\left(\frac{E'Q_o^3 t^4}{\mu'}\right)^{1/9}$ |
| storage/ toughness (K) | $\left(\frac{K'^6}{E'^6 Q_o t}\right)^{1/5}$ | $\left(\frac{E'Q_o t}{K'}\right)^{2/5}$ |
| leak-off/ viscosity (\tilde{M}) | $\left(\frac{\mu'^4 C'^6}{E'^4 Q_o^2 t^3}\right)^{1/16}$ | $\left(\frac{Q_o^2 t}{C'^2}\right)^{1/4}$ |
| leak-off/ toughness (\tilde{K}) | $\left(\frac{K'^8 C'^2}{E'^8 Q_o^2 t}\right)^{1/8}$ | $\left(\frac{Q_o^2 t}{C'^2}\right)^{1/4}$ |

Table 2. Parameters \mathcal{P}_1 and \mathcal{P}_2 for the two storage scalings (viscosity and toughness) and the two leak-off scalings (viscosity and toughness).

| | \mathcal{P}_1 | \mathcal{P}_2 |
|-------------|---|---|
| M | $\mathcal{K}_m = \left(\frac{K'^{18} t^2}{\mu'^5 E'^{13} Q_o^3}\right)^{1/18}$ | $\mathcal{C}_m = \left(\frac{C'^{18} E'^4 t^7}{\mu'^4 Q_o^6}\right)^{1/18}$ |
| K | $\mathcal{M}_k = \left(\frac{\mu'^5 Q_o^3 E'^{13}}{K'^{18} t^2}\right)^{1/5}$ | $\mathcal{C}_k = \left(\frac{C'^{10} E'^8 t^3}{K'^8 Q_o^2}\right)^{1/10}$ |
| \tilde{M} | $\mathcal{K}_{\tilde{m}} = \left(\frac{K'^{16} t}{E'^{12} \mu'^4 C'^2 Q_o^2}\right)^{1/16}$ | $\mathcal{S}_{\tilde{m}} = \left(\frac{\mu'^4 Q_o^6}{E'^4 C'^{18} t^7}\right)^{1/16}$ |
| \tilde{K} | $\mathcal{M}_{\tilde{k}} = \left(\frac{\mu'^4 E'^{12} C'^2 Q_o^2}{K'^{16} t}\right)^{1/4}$ | $\mathcal{S}_{\tilde{k}} = \left(\frac{K'^8 Q_o^2}{E'^8 C'^{10} t^3}\right)^{1/8}$ |

The solution regimes can be conceptualized in a rectangular phase diagram $M\tilde{K}\tilde{M}$ shown in Figure 2. Each of the *four primary regimes* (M, K, \tilde{M} , and \tilde{K}) of hydraulic fracture propagation corresponding to the vertices of the diagram is dominated by only one component of fluid global balance while the other can be neglected (i.e. respectively $\mathcal{P}_1 = 0$, see Table 2) and only one dissipative process while the other can be neglected (i.e. respectively $\mathcal{P}_2 = 0$, see Table 2). The solution for each primary regime has the important property that it evolves with time t according to a power law. In particular, the fracture radius R evolves in these regimes according to $R \sim t^\alpha$ where the exponent α depends on the regime of propagation: $\alpha = 4/9, 2/5, 1/4, 1/4$ in the M-, K-, \tilde{M} -, \tilde{K} - regime, respectively.

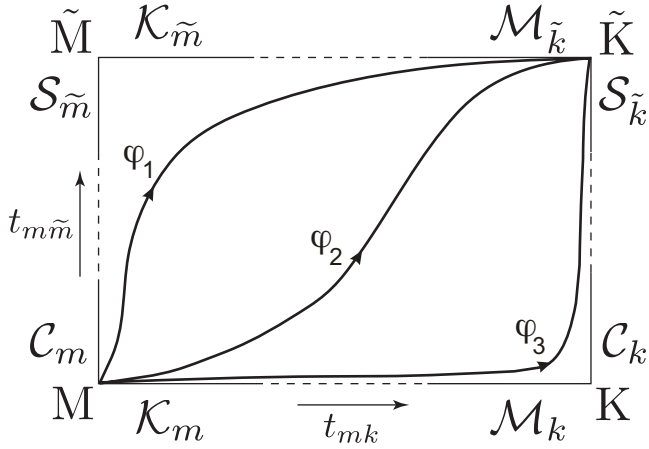


Figure 2. Parametric space.

The regime of propagation evolves with time, since the parameters \mathcal{M} 's, \mathcal{K} 's, \mathcal{C} 's and \mathcal{S} 's depend on t . With respect to the evolution of the solution in time, it is useful to locate the position of the state point in the $M\tilde{K}\tilde{M}$ space in terms of the dimensionless times $\tau_{mk} = t/t_{mk}$, $\tau_{m\tilde{m}} = t/t_{m\tilde{m}}$, where the time scales are defined as

$$t_{mk} = \left(\frac{\mu^{15} E^{13} Q_o^3}{K^{18}} \right)^{1/2}, \quad t_{m\tilde{m}} = \left(\frac{\mu^{14} Q_o^6}{E^{14} C^{18}} \right)^{1/7} \quad (9)$$

Indeed, the parameters \mathcal{M} 's, \mathcal{K} 's, \mathcal{C} 's and \mathcal{S} 's can be simply expressed in terms of these times according to

$$\mathcal{K}_m = \mathcal{M}_k^{-5/18} = \tau_{mk}^{1/9}, \quad \mathcal{C}_m = \mathcal{S}_{\tilde{m}}^{-8/9} = \tau_{m\tilde{m}}^{7/18} \quad (10)$$

and, therefore, the dimensionless times τ 's define evolution of the solution along the respective edges of the rectangular space $M\tilde{K}\tilde{M}$. Furthermore, the evolution of the solution regime in the $M\tilde{K}\tilde{M}$ space takes place along a trajectory corresponding to a constant value of the parameter φ , which is related to the ratios of characteristic times

$$\varphi = \frac{E^{11} \mu^3 C^{14} Q_o}{K^{14}}, \quad \varphi^{9/14} = \frac{t_{mk}}{t_{m\tilde{m}}} \quad (11)$$

(Examples of such trajectories are depicted in Fig. 2.)

In view of the dependence of the parameters \mathcal{M} , \mathcal{K} , \mathcal{C} , and \mathcal{S} on time, see (10), it becomes obvious that the M-vertex corresponds to the origin of time, and the \tilde{K} -vertex to the end of time (except for an impermeable rock). Thus, given all the problem parameters which completely define the number φ ($0 \leq \varphi \leq \infty$), the system evolves with time (say time τ_{mk}) along a φ -trajectory, starting from the M-vertex (viscosity-storage dominated regime: $\mathcal{K}_m = 0$, $\mathcal{C}_m = 0$) and ending at the \tilde{K} -vertex (toughness-leak-off dominated regime: $\mathcal{M}_{\tilde{k}} = 0$, $\mathcal{S}_{\tilde{k}} = 0$). For small values of φ (i.e., for small values of the ratio $t_{mk}/t_{m\tilde{m}}$), the trajectory is attracted by the K-vertex, and conversely for large values of φ the trajectory is attracted by the \tilde{M} -vertex.

The evolution of the fracture in the phase diagram $M\tilde{K}\tilde{M}$ is in part linked to the multiscale nature of the tip asymptotes (Garagash et al. 2007), in particular to the transition from the viscosity edge $M\tilde{M}$ to the toughness edge $K\tilde{K}$ (Madyarova & Detournay 2007). Along the viscosity edge, the tip aperture progressively changes from $w \sim s^{2/3}$ at the M-vertex to $w \sim s^{5/8}$ at the \tilde{M} -vertex (Adachi & Detournay 2007).

An analysis of the range of physical parameters shows that most hydraulic fracturing treatments spend their describable lives in the viscosity-dominated regime. Consider, for example, the typical set of parameters: $Q_o = 0.05 \text{ m}^3/\text{s}$, $E = 15 \text{ GPa}$, $\nu = 0.2$, $K_{Ic} = 0.5 \text{ MPa}\cdot\text{m}^{1/2}$, $\mu = 0.2 \text{ Pa}\cdot\text{s}$, $C_l = 10^{-5} \text{ m}\cdot\text{s}^{-1/2}$. The corresponding time scales are $t_{mk} \simeq 3 \text{ h}$ and $t_{m\tilde{m}} \simeq 3.7 \text{ h}$; also $\varphi \simeq 0.72$. With a treatment time of order $O(1\text{h})$, the fracture propagates for the most part in the viscosity-dominated regime, according to numerical simulations (Madyarova & Detournay 2007). The conditions, for which viscous dissipation is much larger than the rate at which energy is expended in the creation of new surfaces in the rock, depend in principle on two parameters, namely τ_{mk} and φ . However, computations indicate that the fracture evolves along the viscosity edge $M\tilde{M}$ when $\tau_{mk} \lesssim 1$.

4 ANALYTICAL SOLUTION AT M-VERTEX

To facilitate the physical interpretation of the solution, we introduce scaling factors that do not depend on time. Thus, let $\bar{\varepsilon} = \varepsilon_m(t_{mk})$ and $\bar{L} = L_m(t_{mk})$, using (9) to eliminate t_{mk} in the expressions of ε_m and L_m found in Table 1 (with the subscript m denoting the M-scaling)

$$\bar{\varepsilon} = \left(\frac{K^{16}}{Q_o \mu^4 E^{15}} \right)^{1/2}, \quad \bar{L} = \frac{Q_o \mu^4 E^{13}}{K^{14}} \quad (12)$$

Using (12) in the general scaling relationships (8), it is possible to show that the scaled solution $\mathcal{F} = \{\Omega, \Pi, \gamma\}$ can be expressed in the form $\mathcal{F}(\rho, \tau; \varphi)$, where $\tau = \tau_{mk} = t/t_{mk}$. Furthermore, $\mathcal{F}(\rho, \tau; \varphi)$ tends towards the M-vertex solution when τ tends

to 0, irrespective of the value of φ . In the time-dependent scaling, the M-vertex solution can be expressed as

$$\gamma = \gamma_{mo} \tau^{4/9}, \quad \Omega = \Omega_{mo}(\rho) \tau^{1/9}, \quad \Pi = \Pi_{mo}(\rho) \tau^{-1/3} \quad (13)$$

where a first order approximation of the self-similar solution γ_{mo} , $\Omega_{mo}(\rho)$, $\Pi_{mo}(\rho)$ is given by Savitski & Detournay (2002)

$$\Omega_{mo} \simeq \gamma_{mo} \left[\frac{\sqrt{70}}{3} C_1 + \frac{4\sqrt{5}}{9} C_2 (13\bar{\rho} - 6) \right] (1 - \rho)^{2/3} + \frac{8B}{\pi} [(1 - \rho)^{1/2} - \rho \arccos \rho] \quad (14)$$

$$\Pi_{mo} \simeq A_1 \left[\omega_1 - \frac{2}{3(1 - \rho)^{1/3}} \right] - B \left(\ln \frac{\rho}{2} + 1 \right) \quad (15)$$

with $\gamma_{mo} \simeq 0.696$, $A_1 \simeq 0.3581$, $B \simeq 0.09269$, $\omega_1 \simeq 2.479$, $C_1 \simeq 0.6846$, $C_2 \simeq 0.07098$.

5 EXPERIMENTS NEAR THE M-VERTEX

Viscosity-dominated laboratory experiments were performed in order to validate the M vertex solution. The experiments make use of a polyaxial reaction frame (used only for uniaxial loading in this case) which is specially-designed to allow loading parallel to the direction of fracture opening while maintaining the transparency of the system (Fig. 3). In this way the formation of fluid lag can be limited by application of the stress σ_o , while still permitting the growing fracture to be monitored continuously using a digital video camera. This capability relies both on a PMMA lower platen, which also serves as a light source, and on a transparent PMMA upper reaction plate. The location of the fracture front is then determined directly from the video images, and furthermore the fracture opening w is measured from analysis of grayscale images of the growing fracture according to (Bunger 2006)

$$w(x, y) = k \log_{10} \frac{P_o(x, y)}{P(x, y)}, \quad (16)$$

where P_o and P are grayscale pixel values ($0 \leq P, P_o \leq 256$), with $P(x, y)$ corresponding to the value at a location (x, y) within the fluid filled portion of the fracture and $P_o(x, y)$ giving the value at the same location prior to fracture growth. Here k is a calibration factor determined using fluid-filled wedges for which the opening w is known. It has been demonstrated

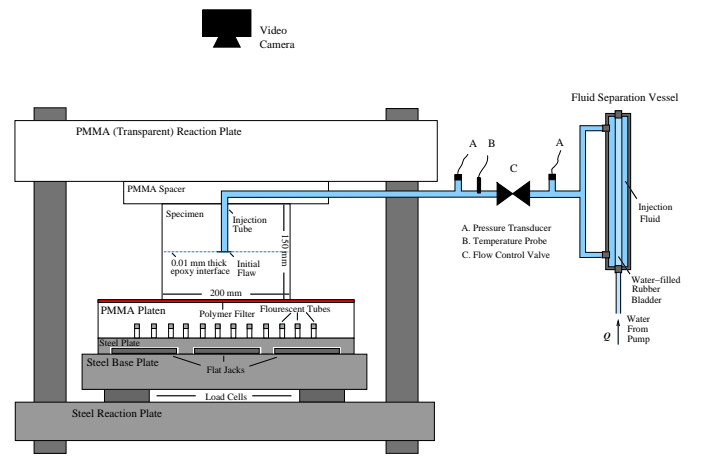


Figure 3. Experimental setup.

that this method is capable of measuring the full-field fracture opening to within an accuracy of 10%, provided that all lighting conditions are carefully controlled (Bunger 2006).

Circular hydraulic fractures were driven along a 0.01 mm thick epoxy-bonded interface between two, 200 x 200 x 75 mm Polymethyl Methacrylate (PMMA) blocks using an aqueous solution of water, blue food dye, and glucose. Fractures were initiated from a 1 mm groove at the base of the 8 mm diameter injection hole. Results are presented for one representative experiment. The plane strain modulus for the PMMA specimen has been determined from uniaxial compression experiments and is given by $E' = 3930$ MPa. The fracture toughness of the epoxy-interface bond has been determined from low viscosity fluid-driven fracture analysis, which is described in detail by Bunger (2006), and is given by $K_{Ic} = 0.38$ MPa $m^{1/2}$. At the temperature at which this experiment was performed, the fluid viscosity is 28.9 Pa s as determined by measurement with a Canon-Fenske type viscometer. Fluid was injected at a nominal rate of $Q_o = 0.04$ mL/s, but the injection rate was not constant and is therefore determined from the pressure drop across the flow-control valve using a test-by-test calibration method that ensures the closest possible satisfaction of global volume balance based on integration of the full-field fracture opening measurements (Bunger et al. 2005). Prior to and during fluid injection, the specimen was loaded so that $\sigma_o = 14.5$ MPa, which was sufficient to prevent formation of a visible lag between the fluid and fracture fronts, as shown in the photograph of the growing fracture in Figure 4. Note that the fracture maintained its horizontal orientation in spite of the uniaxial compressive vertical loading because it was initiated along a low-toughness interface.

The opening as a function of the normalized radial positions $\rho = r/R$ is shown in Figure 5. Here the opening is measured based on image analysis of 4 video frames for which the fracture radii were $R = 27, 31, 36,$ and 40 mm and the corresponding

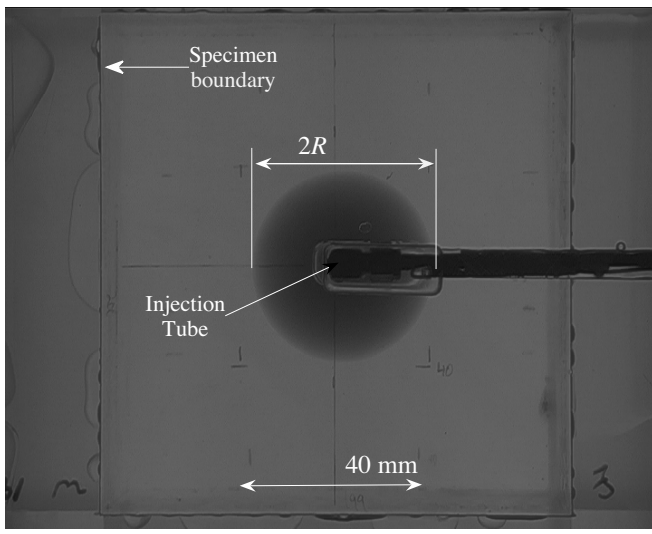


Figure 4. One frame from the video of the growing fracture ($R = 40$ mm), after Bungler & Detournay (2007).

times were $t = 6, 8, 10,$ and 14 s, respectively. The dimensionless viscosity is computed for each of these snapshots to be $\mathcal{M}_k = 6.0, 5.5, 5.0,$ and $4.7,$ respectively, which indicates that the fracture propagates in the viscosity-dominated regime throughout this portion of its lifetime. For each image, the opening is measured over the fluid-filled portion of the fracture along 16 radial lines and the average is taken. Then, scaling the opening according to (8) and (12), the experimental opening is expressed in the dimensionless form Ω_{mo} . Strong agreement between the experimental and analytical results is demonstrated over the outer 60% of the fracture, which is the region that can be clearly viewed in the images.

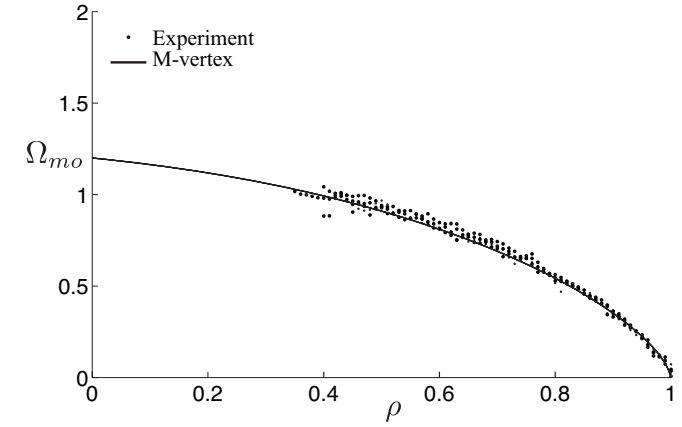


Figure 5. Experimental results compared to the M-vertex solution.

The experimental fracture radius, normalized according to (12), gives a mean value of $\gamma_{mo}^{exp} = 0.62$ with a standard deviation of 0.01. This value is 11% smaller than the analytical value (0.696). This small discrepancy can most likely be traced to the non-constant injection rate (i.e. for the four snapshots used here $Q_o = 0.040, 0.036, 0.040,$ and 0.046 mL/s). Nonetheless, these results further uphold the

ability of the M-vertex solution, under appropriate conditions, to predict hydraulic fracture behavior.

6 NUMERICAL SOLUTION AT M-VERTEX

Finally, we show that accurate numerical solutions of the hydraulic fractures propagating in the viscosity-dominated regime can be achieved, provided that the appropriate tip asymptotes are implemented in the simulator. Here, however, we restrict considerations to the M-vertex conditions.

The numerical solutions were computed with the planar hydraulic fracture code MALIKA (Peirce & Detournay 2007), which is briefly described below. The algorithm is built on a fixed computational grid consisting of a uniform mesh of rectangular constant displacement discontinuity (DD) elements for the elasticity computations Crouch & Starfield (1983), coupled with a five node finite difference stencil for the fluid flow calculations Siebrits & Peirce (2002). The computational scheme further relies on dividing the fracture into two regions, the “Channel” representing the main part of the fracture, and the “Tip,” which is under the asymptotic umbrella, and on iterating at each new time step between the solution in the Channel and that in the Tip. In fact, the Channel corresponds to the contiguous set of fully-filled elements, while the Tip is the set of partially filled elements at the periphery of the fracture. Tip elements exchange fluid only with Channel elements. Figure 6 illustrates the computed footprint of a radial fracture after 25 steps of propagation on a square mesh (see below for further details); the “Channel” and “Tip” elements are colored in green and brown/red, respectively.

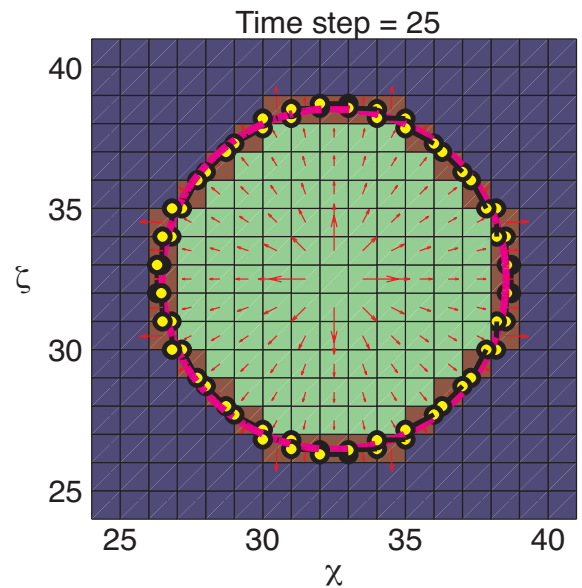


Figure 6. Footprint of fracture at time step 25.

Determining the solution in the Channel requires solving a system of non-linear equations obtained from discretizing the lubrication and elasticity equa-

tions, which are formulated in terms of the constant apertures of the DD elements as the primary unknowns. The solution in the Tip involves computing the location of the front in the partially filled elements, using the tip asymptotic volume and the current volume of fluid stored in the tip elements; the appropriate asymptotic behavior relies on the tip velocity, which is extrapolated from the fluid velocity at the Channel/Tip interface. The local computation of the front position as well as that of the mean aperture of the tip elements is made possible by the one-dimensional nature of the tip asymptote.

Figures 6-9 compare the results of computations carried out with MALIKA for conditions that forces the fracture to evolve at the M-vertex, with the corresponding semi-analytical solution (14)-(15). At the M-vertex, there is no time scale in view of the multiplicative power law dependance of the solution upon time; in other words, the time is here arbitrary. For the example considered, we used square elements with $\Delta\chi = \Delta\zeta = 1$; the injection point is here located at $\chi = \zeta = 32.5$.

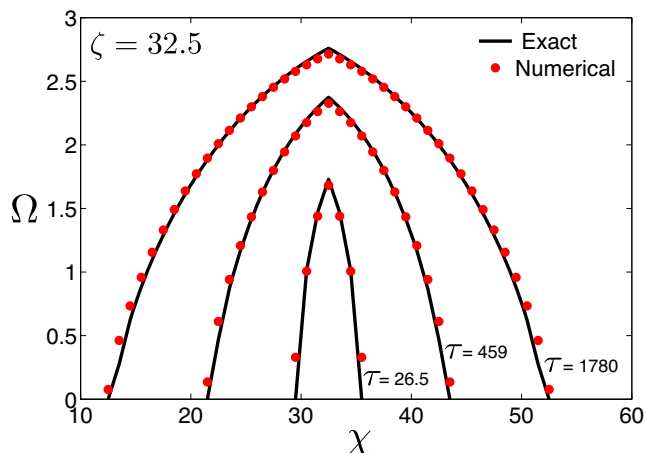


Figure 7. Comparison of computed crack aperture with the exact solution.

In Figure 6 we plot the fracture footprint after 25 time steps which corresponds to $\tau = 26.5$. The local fluid velocity vectors are indicated by the scaled red arrows while the exact fracture front is indicated by the magenta circle. The approximate front positions are indicated by the yellow circles joined by the black line segments. Even for this relatively coarse mesh, the numerical solution is able to locate the circular fluid front relatively accurately.

In Figure 7 we plot the cross section of the width surface $\Omega(\chi, \zeta)$ with the plane $\zeta = 32.5$ for both the numerical solution (solid circles) and the exact solution (solid line), at three different times. The close agreement between these two solutions, for the three levels of discretization is apparent. In Figure 8 we plot a similar cross section through the fluid pressure surface $\Pi(\chi, \zeta)$ for both the numerical pressure (solid circles) and the exact pressure (solid line). In Figure 9 we compare the numerical fracture radius

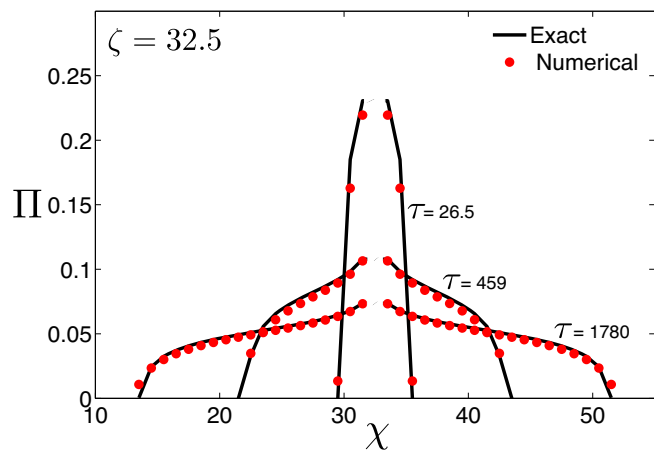


Figure 8. Comparison of computed net pressure with the exact solution.

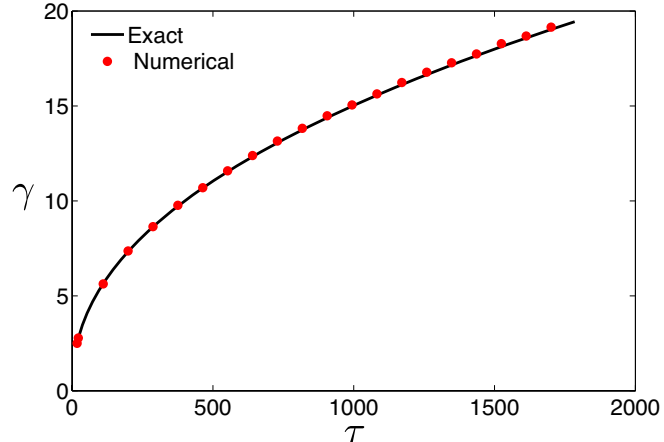


Figure 9. Comparison of fracture radius history (numerical solution plotted every 20 time steps) with the exact solution.

$\gamma(\tau)$ computed by averaging the interception points between the approximate front segments and the element boundaries over the whole perimeter of the fracture.

7 CONCLUSIONS

Using scaling arguments, we have shown that hydraulic fractures engineered to stimulate underground hydrocarbon reservoirs typically propagate in the viscosity dominated regime. Under these conditions, the fractures are characterized by a tip behavior that differs from the classical square root asymptote of linear elastic fracture mechanics. While restricting considerations to the no leak-off case, we have not only demonstrated the physical reality of the M-vertex solution (storage-viscosity-dominated regime) but also the ability to accurately compute fracture propagation under these conditions by embedding the relevant tip asymptote in the numerical simulator.

ACKNOWLEDGEMENTS

AB and ED acknowledge the donors of the American Chemical Society Petroleum Research Fund for

partial support of this research, and AP acknowledge support from the NSERC Discovery Grant Program. The authors also thank Schlumberger for support. Finally, the authors recognize the intellectual contribution of Drs. J. Adachi, D. Garagash, and A. Savitski.

REFERENCES

- Abou-Sayed, A. (1994). Safe injection pressures for disposing of liquid wastes: a case study for deep well injection (SPE/ISRM-28236). *Proc. 2nd SPE/ISRM Rock Mechanics in Petroleum Engineering*, Balkema, pp. 769–776.
- Adachi, J. and E. Detournay (2002). Self-similar solution of a plane-strain fracture driven by a power-law fluid. *Int. J. Numer. Anal. Methods Geomech.* 26:579–604.
- Adachi, J. and E. Detournay (2007). Plane-strain propagation of a fluid-driven fracture in a permeable medium. *Eng. Fract. Mec.*. Submitted.
- Batchelor, G. (1967). *An Introduction to Fluid Dynamics*. Cambridge UK: Cambridge University Press.
- Bunger, A. P. (2006). A photometry method for measuring the opening of fluid-filled fractures. *Meas. Sci. Technol.* 17:3237–3244.
- Bunger, A. and E. Detournay (2007). Early time solution for a penny-shaped hydraulic fracture. *ASCE J. Eng. Mech.* 133.
- Bunger, A. P. and E. Detournay (2007). The tip region in fluid-driven fracture experiments. *J. Mech. Phys. Solids*. In preparation.
- Bunger, A. P., E. Detournay, D. I. Garagash, and A. P. Peirce (2007). Numerical simulation of hydraulic fracturing in the viscosity-dominated regime. In *Proc. 2007 SPE Hydraulic Fracturing Technology Conference*. SPE 110115.
- Bunger, A., R. Jeffrey, and E. Detournay (2005). Application of scaling laws to laboratory-scale hydraulic fractures. In *Alaska Rocks 2005*. Published on CD-ROM, ARMA/USRMS 05-818.
- Crouch, S. and A. Starfield (1983). *Boundary Element Methods in Solid Mechanics*. London: Allen and Unwin.
- Desroches, J., E. Detournay, B. Lenoach, P. Papanastasiou, J. Pearson, M. Thiercelin, and A.-D. Cheng (1994). The crack tip region in hydraulic fracturing. *Proc. Roy. Soc. London, Ser. A* 447:39–48.
- Detournay, E. (2004). Propagation regimes of fluid-driven fractures in impermeable rocks. *Int. J. Geomechanics* 4(1):1–11.
- Detournay, E. and D. Garagash (2007). Scaling laws for a radial hydraulic fracture propagating in a permeable rock. *Proc. Roy. Soc. London, Ser. A*. To be submitted.
- Economides, M. and K. Nolte (Eds.) (2000). *Reservoir Stimulation* (3rd ed.). Chichester UK: John Wiley & Sons.
- Garagash, D. (2006). Transient solution for a plane-strain fracture driven by a power-law fluid. *Int. J. Numer. Anal. Methods Geomech.* 30(14):1439–1475.
- Garagash, D. and E. Detournay (2005, November). Plane-strain propagation of a fluid-driven fracture: Small toughness solution. *ASME J. Appl. Mech.* 72:916–928.
- Garagash, D. I., E. Detournay, and J. Adachi (2007). The tip region of a fluid-driven fracture in a permeable elastic medium. *J. Mech. Phys. Solids*. In preparation.
- Jeffrey, R. and K. Mills (2000). Hydraulic fracturing applied to inducing longwall coal mine goaf falls. In *Pacific Rocks 2000*, Rotterdam, pp. 423–430. Balkema.
- Khristianovic, S. and Y. Zheltov (1955). Formation of vertical fractures by means of highly viscous fluids. In *Proc. 4th World Petroleum Congress, Rome*, Vol. II, pp. 579–586.
- Lister, J. (1990). Buoyancy-driven fluid fracture: The effects of material toughness and of low-viscosity precursors. *J. Fluid Mech.* 210:263–280.
- Lister, J. and R. Kerr (1991). Fluid-mechanical models of crack propagation and their application to magma transport in dykes. *J. Geophys. Res.* 96(B6):10,049–10,077.
- Madyarova, M. and E. Detournay (2007). Fluid-driven penny-shaped fracture in permeable rock. *Int. J. Numer. Anal. Methods Geomech.*. Submitted.
- Mitchell, S., R. Kuske, and A. Peirce (2006). An asymptotic framework for the analysis of hydraulic fractures: the impermeable case. *ASME J. Appl. Mech.*. In press.
- Murdoch, L. (2002). Mechanical analysis of idealized shallow hydraulic fracture. *J. Geotech. Geoenviron.* 128(6): 488–495.
- Peirce, A. P. and E. Detournay (2007). An Eulerian moving front algorithm with weak form tip asymptotics for modeling hydraulically driven fracture. *Journal of Computational Physics*. To be submitted.
- Pollard, D. and G. Hozlhausen (1979). On the mechanical interaction between a fluid-filled fracture and the earth's surface. *Tectonophysics* 53:27–57.
- Rice, J. (1968). Mathematical analysis in the mechanics of fracture. In H. Liebowitz (Ed.), *Fracture, an Advanced Treatise*, Vol. II, Chap. 3, pp. 191–311. Academic Press.
- Rubin, A. (1995). Propagation of magma-filled cracks. *Ann. Rev. Earth & Planetary Sci.* 23:287–336.
- Savitski, A. and E. Detournay (2002). Propagation of a fluid-driven penny-shaped fracture in an impermeable rock: Asymptotic solutions. *Int. J. Solids Struct.* 39(26):6311–6337.
- Siebrits, E. and A. Peirce (2002). An efficient multi-layer planar 3D fracture growth algorithm using a fixed mesh approach. *Int. J. Numer. Meth. Engng.* 53:691–717.
- Sneddon, I. (1951). *Fourier Transforms*. New York NY: McGraw-Hill.
- Spence, D. A. and P. W. Sharp (1985). Self-similar solution for elastohydrodynamic cavity flow. *Proc. Roy. Soc. London, Ser. A* 400:289–313.